Journal of Materials Chemistry C

ROYAL SOCIETY OF CHEMISTRY

PAPER

View Article Online
View Journal | View Issue

Cite this: J. Mater. Chem. C, 2025, 13, 1972

Multifunctional azo-BODIPY-functionalised upconversion nanoparticles as sensors of hypoxia in biological environments†

Jingke Yao,[hi] Silvia Simón-Fuente,[b] Gabriel Lopez-Peña,[c] Silvia Gómez-Pastor,[d] Santiago Guisan-Ceinos,[b] Riccardo Marin,[ae] Emma Martín Rodríguez,[cefg] Daniel Jaque,[aeg] Francisco Sanz-Rodríguez,[*dg] Maria Ribagorda[*be] and Dirk H. Ortgies[*aefg]

Received 2nd August 2024,
Accepted 27th November 2024

DOI: 10.1039/d4tc03302g

rsc.li/materials-c

In this work, a hypoxia-sensitive nanoprobe is developed by coating the surface of upconverting core/shell nanoparticles ($NaGdF_4$: 2%Yb^{3+}, 3%Nd^{3+}, 0.2%Tm^{3+}/$NaYF_4$) with a non-fluorescent azo-dye based on a boron-dipyrromethene functionalized azo compound. Azo-dyes are able to quench fluorescence emissions due to their N=N azo bond, which results in the absorption of most visible emissions of the nanoparticles. However, in a biological environment suffering hypoxia, the azo bond is reduced, which allows the recovery of the nanoparticles' upconversion emissions. Thereby a near-infrared excitable sensor with an azo-dye is created and for the first time not only enables excitation *via* NIR at biocompatible 808 nm but also continuous imaging and tracking of the probe in the infrared due to NIR-emissions enabled by the dopant combination since quenching only occurs in the visible. These multifunctional (imaging and sensing) nanoparticles are characterized, their behaviour in reductive and hypoxic environments is determined and the detection of reducing conditions in a hypoxic environment is demonstrated in cells.

Introduction

Hypoxia, or low oxygen levels, is a common characteristic of solid tumours due to their rapid growth and inadequate blood supply.[1] This oxygen deficiency (<3% O_2) leads to a hostile tumour microenvironment, promoting cancer cell survival, resistance to therapy, and aggressive behavior.[2] As a consequence, common therapeutic strategies that rely on reactive oxygen species generation from oxygen are hampered.[3] Therefore, diagnosing hypoxia in tumour biology is crucial for developing targeted therapies. Early localization of hypoxic tumours can improve staging cancer patients and help enhance treatment outcomes.

The most accurate, yet invasive, method for measuring the local O_2 concentration in a tumour makes use of a needle electrode that provides a readout of partial oxygen pressure (pO_2) in the tissue.[4] Up to now, many imaging strategies have been developed to visualise hypoxic tumours such as positron emission tomography (PET),[5] and single-photon emission computed tomography (SPECT).[6] However, PET and SPECT imaging are based on ionising radiation, are expensive, and rely on radiotracers with a stringent supply chain. Therefore, fluorescence-based hypoxia-responsive molecular probes have attracted considerable attention in recent years.[7–11] Under hypoxic conditions, several reductases, such as azoreductases, are overexpressed due to an excess of reducing cofactors, including flavin adenine dinucleotide ($FADH_2$) and nicotinamide adenine dinucleotide (NADH).[12–14] Based on this knowledge, various probes and prodrugs whose fluorescence is sensitive to hypoxic conditions in tumours have been developed, relying on these reductases.

[a] Nanomaterials for BioImaging Group, Departamento de Física de Materiales, Universidad Autónoma de Madrid, C/Francisco Tomás y Valiente 7, 28049 Madrid, Spain. E-mail: dirk.ortgies@uam.es
[b] Facultad de Ciencias, Departamento de Química Orgánica, Universidad Autónoma de Madrid, 28049 Madrid, Spain. E-mail: maria.ribagorda@uam.es
[c] Nanomaterials for BioImaging Group, Departamento de Física Aplicada, Universidad Autónoma de Madrid, C/Francisco Tomás y Valiente 7, 28049 Madrid, Spain
[d] Departamento de Biología, Universidad Autónoma de Madrid, C/Darwin 2, 28049 Madrid, Spain. E-mail: francisco.sanz@uam.es
[e] Institute for Advanced Research in Chemical Sciences (IAdChem), Universidad Autónoma de Madrid, 28049 Madrid, Spain
[f] Instituto de Ciencia de Materiales Nicolás Cabrera, Universidad Autónoma de Madrid, 28049 Madrid, Spain
[g] Nanomaterials for BioImaging Group, Instituto Ramón y Cajal de Investigación Sanitaria IRYCIS, Ctra de Colmenar km 9300, 28034 Madrid, Spain
[h] Ningbo Eye Institute, Ningbo Eye Hospital, Wenzhou Medical University, Ningbo 315040, China
[i] National Engineering Research Center of Ophthalmology and Optometry, Eye Hospital, Wenzhou Medical University, Wenzhou 325027, China

† Electronic supplementary information (ESI) available: Energy scheme of the nanoparticles, DLS, synthesis of the azo-dye and its reduction, NIR imaging, and dark toxicity data. See DOI: https://doi.org/10.1039/d4tc03302g

This includes hypoxia-responsive nitro-functionalized probes,[15–22] as well as hypoxia-responsive azo-functionalized probes.[23–32]

The azo moiety can quench the emission of fluorophores in close proximity through non-radiative processes, either *via* Förster resonance energy transfer (FRET) or non-FRET processes typically associated with the ultrafast *trans*/*cis* isomerization of the –N=N– double bond.[25,33–35] The overexpression of azoreductases in the cellular environment under hypoxia enables the reductive cleavage of the azo bond (–N=N–) of these dyes thereby restoring the emission of the released fluorophore.

The combination of an azocompound with near-infrared (NIR) emitters enable the use of excitation pathways compatible with biological tissues, in contrast to classical dye-based sensors. Rare-earth-doped nanoparticles (RENPs) are particularly suited for this application because depending on the dopants they present the ability to convert two or more NIR photons into one photon of higher energy (typically in the visible range) by upconversion. This makes it possible to excite the sensor in the NIR transparency windows, *i.e.*, wavelength ranges where the photon-tissue interaction is minimal and hence photons can penetrate biological tissues up to a few centimetres. This capability has become a pivotal aspect of Förster resonance energy transfer (FRET) to dyes and photosensitizers from RENPs in close proximity, enabling their indirect excitation with NIR radiation. Thereby the structure of visible-light-absorbing chromophores can be maintained, which usually results in improved photostability and less reactivity in biological media. Furthermore, RENPs generally show good biocompatibility and allow a wide range of surface functionalization, which can help with the biodistribution and transport of organic chromophores that act as biosensors.[36,37]

Although the use of azocompounds as fluorescent quenchers is well-known, to the best of our knowledge, there have been just a few reports employing upconversion-based hypoxia sensors, excited at 980 nm.[38–40] The simple combination of an azo quenching dye and nanoparticles excitable at the biocompatible wavelength of 800 nm would be useful for the development of novel NIR sensors for hypoxia sensing, because reductive cleavage of the azo bond would reestablish the emission properties of the nanoparticles and excitation at 800 nm would impart the nanosensor with improved biocompatibility. We recently described a new family of non-toxic 3-azo-conjugated BODIPY dyes as fluorescent biosensors of hypoxia-like conditions.[41] Herein, we report the preparation and combination of a modified 3-arylazo-BODIPY with a pendant carboxylic acid with upconverting RENPs, discuss their photophysical properties, and demonstrate their employment as NIR probes for hypoxia conditions (Fig. 1). The initial non-emissive azo-conjugated BODIPY is turned on under bioreductive conditions and the recuperation of the sensor's emission is also visualized in HeLa cells by fluorescence imaging techniques.

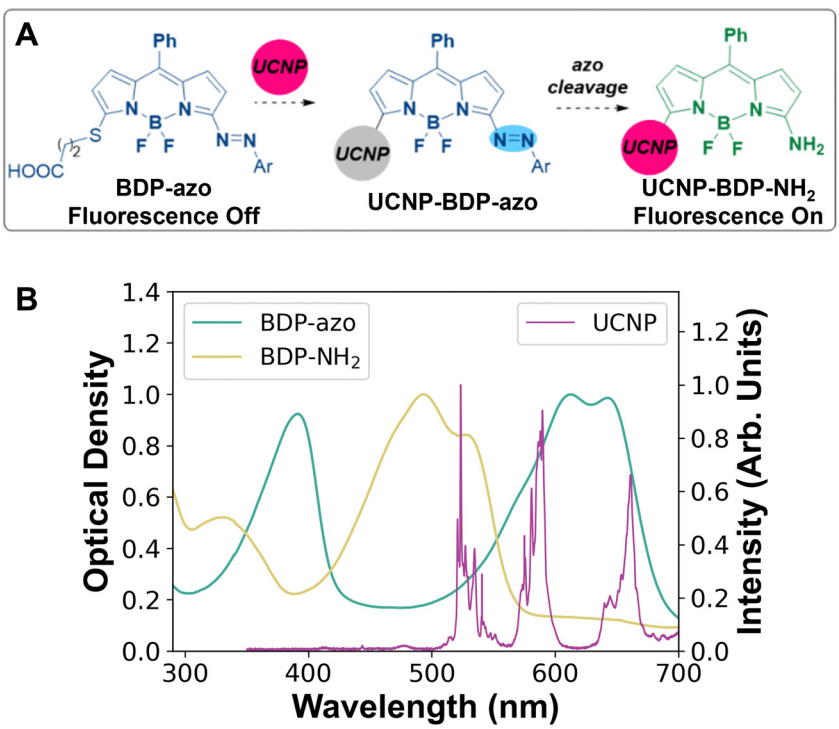

Fig. 1 Schematic depiction of the preparation of UCNP-BDP-azo as NIR fluorescent nanoprobe for hypoxia. (A) Nonfluorescent azo-BODIPY (BDP-azo) is bound to PEG-functionalized upconverting nanoparticles (UCNP) resulting in nanoparticles with quenched visible emissions (UCNP-BDP-azo). Under hypoxia conditions azo cleavage occurs and the resulting nanoparticles (UCNP-BDP-NH_2) have their visible emission restored [drawn with ChemDraw 22]. (B) Extinction and emission spectra demonstrating the overlap of the dye's absorbance (BDP-azo, turquoise line) with the upconversion emission of the UCNPs (magenta line). The absorbance of the product of azo reductive cleavage, BDP-NH_2 (yellow line), in contrast does only partially affect the UCNP's emissions.

Experimental

Synthetic procedures

All materials were used as received without further purification. Y_2O_3 (99.99%), Gd_2O_3 (99.99%), Yb_2O_3 (99.9%), Nd_2O_3 (99.9%), Tm_2O_3 (99.99%), hexane (97%), 1-octadecene (ODE, >90%), nitrosonium tetrafluoroborate ($NOBF_4$, 97%), hydrochloric acid (37%), 1-ethyl-3-(3′-dimethylaminopropyl)carbodiimide HCl (EDC·HCl, ≥98%), and *N*,*N*-dimethylformamide (DMF) were purchased from Sigma-Aldrich. Phosphate-buffered saline (PBS, pH 7.4), sodium formate (98%), zinc powder (>97%), oleic acid (OA, 90%), and 1-octadecene (ODE, 90%) were purchased from Alfa Aesar. NH_2-PEG_{12}-COOH (≥95%, Thermo Fisher Scientific).

Synthesis of azo dye. We prepared BDP-azo **2** from 3-azo-5-chloro-BODIPY (Cl-BDP-azo) **1**,[41] by a nucleophilic substitution reaction with 3-mercaptopropionic acid in the presence of triethylamine, with an isolated yield of 68%, obtaining a dark blue solid (Fig. S3, ESI†). For details, see the ESI.†

Synthesis of upconversion nanoparticles $NaGdF_4$: 2%Yb^{3+}, 3%Nd^{3+}, 0.2%Tm^{3+} (core). The core particles were synthesized following a modified co-precipitation method. 0.4725 mmol Gd_2O_3, 0.0100 mmol Yb_2O_3, 0.0150 mmol Nd_2O_3, and 0.0025 mmol Tm_2O_3 were added into a 100 mL three-neck round-bottom flask, mixed with 5 mL hydrochloric acid (37%) and 5 mL of distilled water and the cloudy solution was refluxed at 80 °C for 12 h. The now clear solution was slowly dried at 60 °C until excess HCl and water were removed. Next, 10 mL of oleic acid and 20 mL of 1-octadecene were added to the dried precursor. The mixture was heated at 150 °C for 45 min forming a clear solution that was allowed to cool to 50 °C. 2.5 mmol NaOH and 4.0 mmol NH_4F in 10 mL methanol were carefully mixed and rapidly given into the solution and stirred for 40 min. The excess methanol was removed at 65 °C for 1 h and then the temperature was elevated to 290 °C and maintained for 2 h. Finally, the solution was allowed to cool to room temperature and the NPs were precipitated and washed with absolute ethanol twice. The obtained core NPs were dispersed in 10 mL of hexane.

Synthesis of upconversion nanoparticles $NaGdF_4$: 2%Yb^{3+}, 3%Nd^{3+}, 0.2%Tm^{3+}/$NaYF_4$ (core/shell). The core/shell nanoparticles used in this work were synthesised using a modified co-precipitation method. In the first step, 0.5 mmol Y_2O_3 with 5.0 mL hydrochloric acid (37%) and distilled water (5.0 mL) were added to a 100 mL three-neck round-bottom flask. The cloudy solution was refluxed at 80 °C for 12 h, and then excess hydrochloric acid and water were slowly removed at 60 °C. In the second step, oleic acid (4 mL) and 6 mL 1-octadecene were added to the dried precursor, heated at 150 °C for 45 min until a clear solution was formed, and then cooled to 80 °C. 0.4 mL of core NPs in *n*-hexane were injected, and *n*-hexane was evaporated completely and then cooled to 50 °C. 2.5 mmol NaOH and 4 mmol NH_4F in 10 mL of methanol were added to the solution and stirred for 60 min. Next, extra methanol was removed at 65 °C for 1 h. The temperature was increased to 290 °C and kept for 1.5 h. Finally, the solution was cooled to room temperature and the NPs were precipitated and washed twice with acetone. The obtained core–shell NPs were dispersed in hexane (10 mL).

Synthesis of water-dispersible UCNPs@OOC-PEG_{12}-NH_2 (UCNP). In the first step, core/shell NPs (2.5 mL) dispersed in hexane were mixed in a 50 mL centrifuge tube with 2.5 mL of $NOBF_4$ in DMF (0.01 M) at room temperature. The mixture was vortexed until the hexane layer was clear. Subsequently, 20 mL toluene and 20 mL hexane were added to the tube, and the solution was vortexed for 1 min, followed by centrifugation at 6000 rpm for 20 min. The colourless precipitate was collected and dispersed in 5 mL DMF for further use. In the second step, 20 mg $NOBF_4$ stabilized UCNPs in DMF and 4 mg NH_2-PEG_{12}-COOH were added to 3 mL of PBS. The reaction was maintained at room temperature for 12 h and then washed twice with acetone. The obtained UCNPs@OOC-PEG_{12}-NH_2 were dispersed in 3 mL PBS.

Synthesis of water-dispersible UCNP-BDP-azo. UCNPs in 3 mL PBS were added to a mixture of 4.75 mg EDC and 5.75 mg NHS in DMSO (2 mL). The solution was sonicated for 1 h. Subsequently, BDP-azo (8 mg) was added to this solution. The reaction was maintained at room temperature for 12 h. Subsequently, the nanoparticles were collected by centrifugation and washed twice with acetone. The obtained UCNP-BDP-azo were re-dispersed in 3 mL of PBS containing 5 vol% DMSO.

Characterizations

Transmission electron microscopy. The nanoparticles were imaged on carbon-coated copper grids by placing a 10 μL drop of dispersion on them and letting it dry for 5 min. Images were obtained using a JEM1400 Flash (JEOL) microscope operating at an acceleration voltage of 80 kV.

Extinction spectroscopy. The optical extinction spectra were recorded at room temperature with a UV-VIS-NIR spectrophotometer (PerkinElmer Lambda1050) including a sample path and a reference path using a 2 nm step.

Fluorescence spectra. The emission spectra were acquired by use of fibre-coupled 790 nm laser diodes (Lumics) focused on a quartz cuvette containing the different NPs (concentration 1.0 mg mL^{-1}) in hexane or PBS. The optical signal was collected after passing through an 850 nm long-pass filter using an Andor Shamrock 193i spectrometer with an InGaAs CCD camera (Andor iDus DU490A) and spectrally analysed. For the visible spectra the emission was passed through a 750 nm short-pass filter and analysed using a monochromator (iHR320, HORIBA) and a cooled CCD array detector (Synapse, HORIBA).

FTIR spectroscopy. The vibrational (FTIR) spectrum was obtained from 450 to 4000 cm^{-1} with a resolution of 4 cm^{-1} in the transmission mode on a Shimadzu IRSpirit instrument, measuring freshly prepared KBr tablets containing 1 wt% of the sample.

Fluorescence lifetime measurements. An optical parametric oscillator (Quanta Ray) pumped by a frequency-tripled Nd:YAG laser operating at 355 nm provided excitation at 800 nm with 10 ns pulses, an average energy of 0.2 J, and a repetition rate of 10 Hz for room temperature lifetime measurements of the NPs' dispersions (1 mg mL^{-1}). Luminescence was collected and spectrally filtered using a high-brightness monochromator (Shamrock 163 from Andor). Time-evolution curves were

obtained using an infrared photomultiplier (Hamamatsu H1033C) connected to a digital oscilloscope (Le Croy Wave Runner 500).

Dynamic light scattering. Dynamic light scattering spectra were obtained using a Zetasizer Nano ZS instrument (Malvern Panalytical). The samples were prepared with a 0.1 mg mL^{-1} concentration in water contained in a standard 1 cm quartz cuvette. The equipment's illumination source was a 630 nm red laser, and the angle between the sample and detector was 173°.

Cellular experiments

Cell culture. The HeLa human cervical epithelial cell line (used as tumor cell model) was grown in Dulbecco's modified Eagle's medium (DMEM, Cytiva, HyClone, Logan, Utah, USA) supplemented with fetal calf serum (FCS 10%, Gibco) and 0.5% antibiotics (penicillin G [10 000 U mL^{-1}] and streptomycin sulfate [10 000 mg mL^{-1}] (Gibco)). DMEM supplemented with FCS and antibiotics will be referred to as complete medium. The cells were grown in a Thermo FORMA Direct Heat cell incubator (Thermo Scientific) with a 5% CO_2 atmosphere, 95% relative humidity, and a constant temperature of 37 °C.

Nanoconjugate administration. Stock solutions of both UCNP and UCNP-BDP-azo NPs were prepared in DMSO (Panreac) at a concentration of 1 mg mL^{-1}. The work solutions were obtained by dissolving the compounds in complete medium. The final concentration of DMSO was always lower than 0.5% (v/v), and the lack of toxicity of this solvent for the cells was also tested and confirmed. All the treatments were performed when cultures reached around 60–70% of confluence.

Cytotoxicity tests. The viability of HeLa cells exposed to UCNP and UCNP-BDP-azo NPs was analysed 24 h after treatments using the MTT assay. Following treatments, 3-(4,5-dimethylthiazol-2-yl)-2,5-diphenyltetrazolium bromide (MTT) solution was added to each well at a concentration of 0.5 ng mL^{-1}, and plates were incubated at 37 °C for 2 h. The resulting formazan crystals were dissolved by the addition of dimethyl sulfoxide and the absorbance was measured at 542 nm. Cell viability was estimated as a percentage relative to the mean absorption obtained from the control cells (not incubated with UCNPs and UCNP-BDP-azo; 100% viability).

Anoxia experiments. Live cell imaging studies in a multiphoton confocal microscopy were performed using HeLa cells gradually subjected to an oxygen free atmosphere. It has been reported that the thin cover glass placed over a cell culture plate blocks the oxygen supply to the cells beneath it, resulting in a decrease of oxygen concentration and generating anoxia or different levels of hypoxia.[41,42] For this purpose, HeLa cells were seeded on coverslips 24–48 h before the treatments. Two hours prior to confocal analysis, the cells were incubated with UCNP and UCNP-BDP-azo. The cells were then washed with PBS and the coverslips placed and sealed with nail varnish on glass slides. Images were taken with different excitation and emission wavelengths at different times, from 0 to 60 min (at 10 min intervals).

Multiphoton confocal microscopy. All images were obtained on Zeiss LSM 780 upright confocal – multiphoton. The Zeiss microscope has the following illumination sources: Coherent Chameleon Vision-S Coherent laser (75 fs pulse) 690–1050 nm. Diode 405 nm. Argon ion laser: 458, 488, 514 nm. High power diode 561 nm. Diode 633 nm and an Xcite fluorescence lamp with the following epi-fluorescence filters: DAPI: Fs49 Ex G365 FT 395 Em BP 445/50. GFP: Fs 38 Ex BP 470/40 FT 495 Em BP 525/50. Net: FS 43 Ex BP 550/25 FT 570 Em BP 605/70.

Results and discussion

Core/shell nanoparticles were prepared by a modified co-precipitation method (see the Experimental section for details).[43,44] We synthesised $NaGdF_4$: 2%Yb^{3+}, 3%Nd^{3+}, 0.2%Tm^{3+} (core) and $NaGdF_4$: 2%Yb^{3+}, 3%Nd^{3+}, 0.2%Tm^{3+}@$NaYF_4$ (core/shell) nanoparticles. These small nanoparticles with intense upconversion emissions, excitable in the first NIR transparency window, were also endowed with dispersibility in biological media allowing them to reach a hypoxic environment. Additionally, their stable NIR emissions enabled the visualisation and tracking of the nanoparticles in biological tissues. Their emission mechanism featuring both upconversion and NIR emissions with long photoluminescence lifetime, was described for the first time in 2014.[45] An energy level diagram depicting the different emissions is included in the ESI† (Fig. S1).

The as-prepared core and core/shell nanoparticles were spherical and highly monodispersed, with average sizes of (12 ± 2) nm and (17 ± 2) nm, respectively (Fig. 2A and B). The optical properties of the synthesised core and core/shell structures were investigated. As expected, the emission intensities of both upconversion and downshifting (*i.e.*, NIR) luminescence of core/shell nanoparticles were stronger than those of core-only, due to the reduction in surface defects by the inert $NaYF_4$ shell (Fig. 2C and D).[46,47] Additionally, DLS experiments in hexane were performed (Fig. S2, ESI†), and the results are in concordance with the TEM sizes, providing a mean diameter of 11 nm for the core nanoparticles and 14 nm for the core–shell nanoparticles, which are very close to the actual sizes of the nanoparticles. Moreover, the polydispersity indices (PdI) of the core and core/shell nanoparticles are both 0.2, meaning that both nanoparticles present a monodisperse character (PdI < 0.7).[48]

The BDP-azo fluorescence quencher was prepared following our previous work, from 3,5-dichloro-BODIPY by a two-step protocol followed by nucleophilic addition of 3-mercaptopropionic acid enabling the conjugation to the NPs (see detailed synthesis in Fig. S3, ESI†). This dye was chosen due to the overlap of its absorbance with the NPs' upconversion emission as demonstrated in Fig. 1B. It is noteworthy to mention that the BDP-NH_2, obtained after reductive cleavage of BDP-azo using Zn/HCO_2NH_4 (Fig. S4, ESI†), does not exhibit strong absorbance overlapping with the upconversion emissions. Therefore, the absorption spectra of BDP-azo and free BDP-NH_2 included in Fig. 1B, suggested that under hypoxic conditions, leading to cleavage of the azo-bond, the upconversion emissions should be recovered at least partially. Hence, to convert our NPs into the desired hypoxia sensors, ligand transfer was first performed by exchanging oleic acid on the surface by treating the NPs with $NOBF_4$ to generate BF_4^--stabilised core/shell NPs.[49,50] Second, the

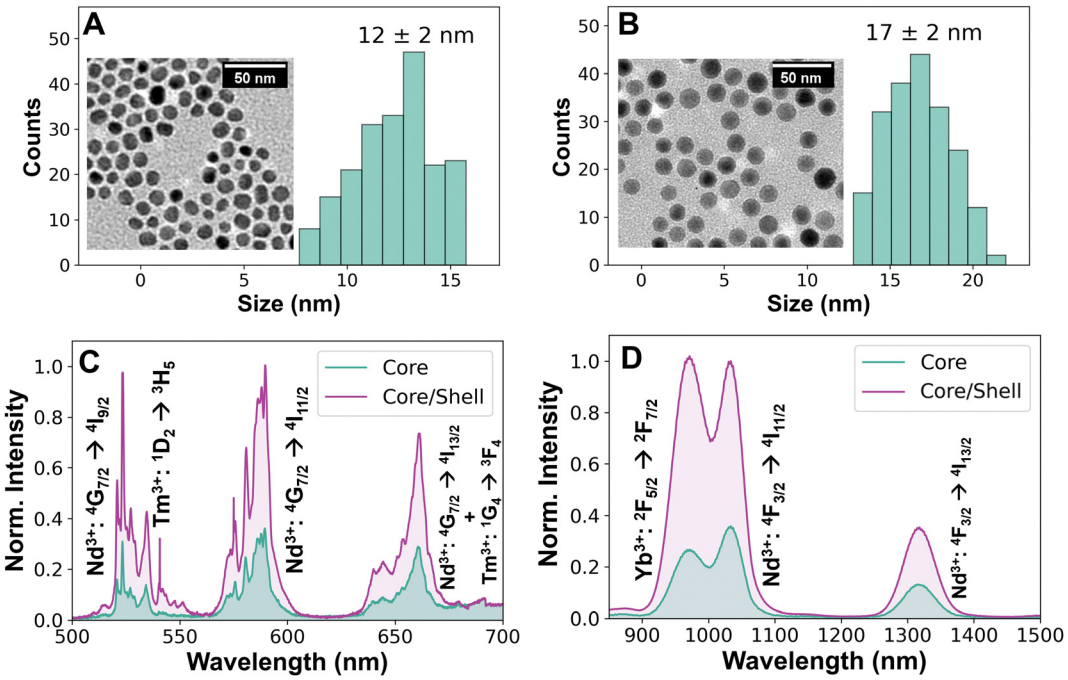

Fig. 2 Characterization of core/shell nanoparticles. (A) TEM image and size distribution of core nanoparticles. (B) TEM and size distribution of core/shell nanoparticles. (C) Emission spectrum of a 1.0 mg mL^{-1} hexane dispersion of upconversion emissions in the visible of core and core/shell nanoparticles excited at 790 nm. (D) Comparison of infrared emissions of a 1.0 mg mL^{-1} hexane dispersion of core and core/shell nanoparticles.

short linker HOOC-PEG_{12}-NH_2 was added to obtain UCNP-PEG (from now on referred to as UNCP for simplicity), binding through the interaction of the negatively charged carboxylate with the surface metal ion on the surface of the NPs, and bearing the amino group for the next step.[51] The polyethylene glycol groups in the linker also improved their dispersibility in phosphate-buffered saline (PBS). Finally, UCNP-BDP-azo was obtained by EDC/NHS (*N*-ethyl-*N*′-(3-(dimethylamino)propyl)carbodiimide/*N*-hydroxysuccinimide) mediated coupling reaction in dimethyl sulfoxide (DMSO).[52]

Characterisation of the final UCNP-BDP-azo revealed spherical and highly monodisperse NPs with an average size of (20 ± 1) nm (Fig. 3A). Their dispersion in DMSO showed a distinct blue colour owing to the strong absorption of BDP-azo (Fig. 3B). This property was also demonstrated in the absorption spectrum of the UCNP (Fig. 3C). After binding BDP-azo to the surface of the UCNP, there were two absorption peaks in the UCNP-BDP-azo, consistent with the absorption bands of free BDP-azo (compare Fig. 1B), while the UCNP-BDP-NH_2 show a broad shoulder around 490 nm associated with BDP-NH_2. Thereby it was demonstrated that the absorption properties of the azo dye were maintained during conjugation to the UCNP.

The surface chemistry of the UCNP was further investigated using FTIR spectroscopy, as shown in Fig. 3D. The double peaks at 2920 and 2854 cm^{-1} indicate the presence of CH_2 in the spectrum of the oleate-capped UCNP (UCNP@OA), and the interaction between the carboxyl group and the positively charged metal atoms on the surface of the nanoparticles resulted in the presence of peaks at 1455 and 1560 cm^{-1} due to the asymmetric and symmetric vibration modes of the $-COO^-$ groups, respectively. After replacing oleic acid with $NOBF_4$, the $-CH_2$ and C=O peaks disappeared and a characteristic peak of BF_4^- appeared at 1084 cm^{-1}. In the FTIR spectrum of UCNP, there was a broad peak at 3400 cm^{-1}, and the vibration of C–O at 1085 cm^{-1} confirmed that the peak at 3400 cm^{-1} was mostly –OH overshadowing the N–H vibration, which indicated that HOOC-PEG_{12}-NH_2 had successfully replaced OA on the surface of the NPs. The decrease in the O–H vibration in UCNP and UCNP-BDP-azo indicated a reduction in the presence of hydrogen bonding to the N–H and a decreased accessibility of water to the carboxylates on the NPs surface once the azo dye was attached. These results indicated the successful preparation of UCNP-BDP-azo.

To evaluate the optical properties of the multifunctional UCNP-BDP-azo as hypoxia sensors, the azo bond was reduced to the amino groups employing ammonium formate and zinc powder in DMSO as a mild source of hydrogen (analogous to Fig. S4, ESI†). After chemical reduction, the colour of UCNP-BDP-azo changed from blue to nearly colourless. Additionally, an optical characterisation of the BDP-azo and BDP-NH_2 molecules was performed, demonstrating that BDP-azo shows two main absorption bands around 370 and 600 nm and BDP-NH_2 shows one broad absorption band around 500 nm (Fig. S5A, ESI†). Additionally, only BDP-NH_2 was able to show a broad emission band around 560 nm when excited at 500 nm (Fig. S5B, ESI†).

The fluorescence emission of UCNP, UCNP-BDP-azo, and UCNP-BDP-NH_2 at a concentration of 1 mg mL^{-1} was investigated. The visible emission of UCNP-BDP-azo was strongly quenched, especially the bands at 523 nm (Nd^{3+}: $^4G_{7/2} \rightarrow {}^4I_{9/2}$),

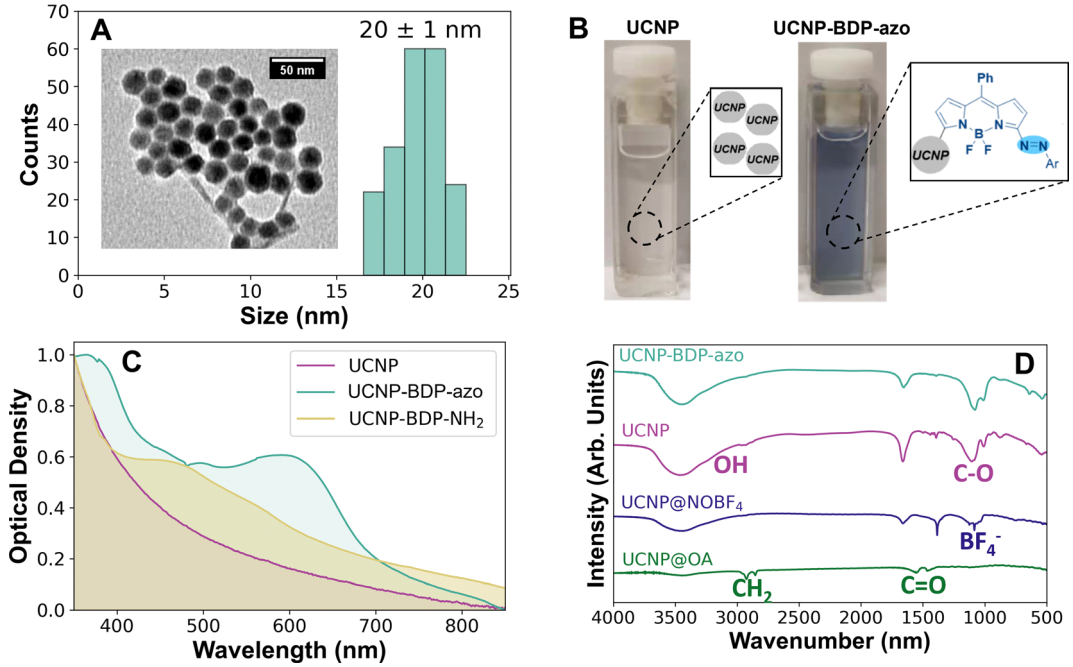

Fig. 3 Characterization of UCNP-BDP-azo. (A) TEM and size distribution of dye-functionalised UCNP-BDP-azo. (B) Cuvette images of UCNPs (left) and UCNP-BDP-azo (right) illustrating the blue colour of UCNP-BDP-azo. (C) Extinction spectra of UCNP (magenta), showing mostly scattering from the nanoparticles, functionalized UCNP-BDP-azo (turquoise), where the absorption of the organic dye is dominating, and the UCNP-BDP-NH_2 (yellow) presenting less extinction, and one broad band associated with BDP-NH_2. (D) FTIR spectra of the nanoparticles during the functionalisation steps towards the UCNP-BDP-azo.

542 nm (Tm^{3+}: $^1D_2 \rightarrow {}^3H_5$), 588 nm ($Nd^{3+}$: $^4G_{7/2} \rightarrow {}^4I_{11/2}$), and 662 nm ($Nd^{3+}$: $^4G_{7/2} \rightarrow {}^4I_{13/2}$ and Tm^{3+}: $^1G_4 \rightarrow {}^3F_4$), because they overlap with the main broad absorption band of BDP-azo, as shown in Fig. 1A.[53] Due to the weaker quenching ability of the BDP-NH_2 dye after reduction, compared to the BDP-azo dye, the emission of UCNP-BDP-NH_2 was not equal to that of bare UCNP but partially recovered (Fig. 4A). These experiments demonstrated that a reductive environment, such as the one found in hypoxia, stopped the quenching of the visible emission of the nanoparticles and led to partial recovery of the upconversion emission of the UCNP. Therefore, the developed UCNP clearly demonstrated their potential as hypoxia-sensitive nanosensors.

The NIR emissions of UCNP, UCNP-BDP-azo, and UCNP-BDP-NH_2 (1 mg mL^{-1}) were also investigated under 800 nm laser irradiation. The NIR emission of UCNP-BDP-azo decreased compared to the UCNP with only PEG on the surface but after the azo reduction, the NIR emission of UCNP-BDP-NH_2 remained stable compared to that of UCNP-BDP-azo (Fig. 4B). These results demonstrate that even though the visible emission of the nanoprobe depend on the reductive conditions in the environment, its NIR emissions are independent of the oxygen levels or presence of reducing enzymes in the tissues. Indeed, this confers our nanosensors with a capability to act as multifunctional (sensing and imaging) contrast agent for deep-tissue imaging and thereby allows their tracking prior and during hypoxia conditions in tissue. Fig. S6 (ESI†) demonstrates the capability for deep-tissue imaging showing a dispersion of UCNP-BDP-NH_2 under 5 mm of lipid-rich phantom tissue. Even though the imaging experiment only employed a low, biocompatible power density (50 mW cm^{-2}) and a short exposure time

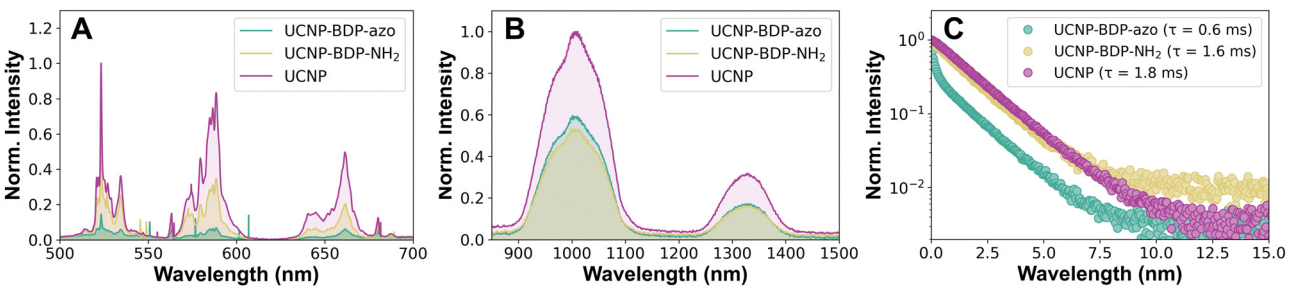

Fig. 4 Change in fluorescence emission of UCNP due to reductive environment. (A) Upconversion emission of dispersions of free UCNP and of UCNP-BDP-azo prior and after reduction to UCNP-BDP-NH_2. While the UCNP-BDP-azo signal is nearly completely quenched respective the free UCNP the signal is practically recovered for UCNP-BDP-NH_2. (B) Emission spectra in the near infrared. The UCN-BDP-azo demonstrate higher NIR emission which is not affected by reduction to UCNP-BDP-NH_2. (C) Fluorescence lifetimes of the three samples measured at 980 nm under 800 nm excitation.

(0.1 s), it still allows to identify the emission from the cuvette. This highlights thereby the potential for *in vivo* imaging in the NIR of our probe, which is a consequence of the particular dopant combination as previously demonstrated.[36,54]

Subsequently, the NIR fluorescence lifetimes of UCNP, UCNP-BDP-azo, and UCNP-BDP-NH_2 (1 mg mL^{-1}) were measured at 980 nm under 800 nm pulsed-laser excitation (Fig. 4C). The fluorescence lifetime obtained from the decay curves of the UCNP was 1.8 ms. For the UCNP-BDP-azo, the fluorescence lifetime decreased to 0.6 ms. This decrease in fluorescence lifetime stems from the FRET process between UCNP and BDP-azo molecules on their surface. After azo reduction, the fluorescence lifetime recovered nearly to its initial value of 1.8 ms. The results showed that FRET, which resulted in partial non-radiative deexcitation by the dye, ceased after the azo reduction had occurred. From these lifetimes, the FRET efficiency can be calculated using eqn (1):

$$\eta = 1 - \frac{\tau_{\text{UCNP-BDP-azo}}}{\tau_{\text{UCNP}}} = 1 - \frac{0.6}{1.8} \approx 67\% \qquad (1)$$

where τ_{UCNP} refers to the fluorescence lifetime of the unfunctionalized UCNP (1.8 ms) and $\tau_{\text{UCNP-BDP-azo}}$ refers to those functionalized with the azo dye (0.6 ms). It is possible to measure the FRET here indirectly because the azo dye absorption band overlaps with the visible emission of the UCNP, which stem from two energy levels, the Nd^{3+} $^4G_{7/2}$ and Tm^{3+} $^1G_4$ level, which are only populated after upconversion involving the Yb^{3+} $^2F_{5/2}$ level, whose lifetime is measured. In addition, when the BDP-azo was reduced, the lifetime of Yb^{3+} at 980 nm returned to its original value. The calculated value indicated a strong FRET efficiency even though an inert shell is present.[55] This indicates that the improvement of the emission intensity due to improvement of the core's surface is overweighing the losses due to the increased distance at which FRET must occur.[56]

Subsequently, the biocompatibility of the nanosensors (Fig. S7, ESI†) was evaluated in cultured cells. The cytotoxicity of UCNP and UCNP-BDP-azo was tested by incubating HeLa cells with different concentrations (2, 10, 20 and 50 μg mL^{-1} in complete medium) of the nanosensors for 2 h. To exclude DMSO toxicity, a control group was incubated with vehicle only (5% DMSO in complete medium). Fig. S7 (ESI†) shows the results of this toxicity experiment 24 hours after treatments, demonstrating no appreciable toxicity, with a maximum decrease in cell viability of 18% after incubation with UCNP-BDP-azo at a concentration of 50 μg mL^{-1}. Therefore, UCNP-BDP-azo showed good biocompatibility, which served as a basis for the following experiments.

Fig. 5 illustrates the study of the hypoxic response of the nanosensors in cell cultures. HeLa cells were incubated with UCNP and UCNP-BDP-azo for 2 h and prepared for analysis by multiphoton confocal microscopy (see Experimental section). To generate the hypoxia environment, before starting the analysis, the coverslips on which the cells were seeded were sealed, depriving them of oxygen and generating an anoxic environment as a model of the hypoxic conditions that the probes might encounter in a tumour environment.[57] This was visualized throughout in different excitation and emission channels in the multiphoton confocal microscope to detect the visible emissions of the UCNP-BDP-NH_2 that should form in that process due to azo group cleavage. Fig. 5A follows the cleavage of the azo bond in UCNP-BDP-azo when exciting in the NIR at 808 nm and *via* direct excitation at 561 nm. Both channels demonstrate an increase in signal intensity in their respective emission range (false green: 508–615 nm, false red: 570–641 nm) over time as illustrated by the intensity diagram in Fig. 5C. The third line of images in Fig. 5A shows the bright-field vision of the cells so that the signal from the top can be localized as stemming from inside the cells.

In the control experiment UCNP without any dye were employed, shown in Fig. 5B. Here the signal fluctuates lightly between images but no increase over time due to the anoxic conditions can be observed, as visualized in Fig. 5C. Interestingly, not only the upconversion excitation (λ_{ex} = 808 nm, first row) results in emissions but also a direct excitation of the UCNP at 561 nm (second row) leading to weak emissions from the Nd^{3+} $^4G_{7/2}$ level is observed. This signal stemming from the endocytosed nanoparticles was possible to observe due to aggregation inside endosomes/vesicles improving their absorbance.[36] Comparison of the intensities under these conditions with the broken UCNP-BDP-azo shows a clear difference in the signal, illustrating the emission recovery over time due to removal of the quenching azo group. A series of control images of cells without nanoparticles is included as Fig. S8 (ESI†) showing no relevant emissions. These results demonstrated that the UCNP-BDP-azo can be employed as a hypoxia sensitive probe in cells because its visible emission are recovered in an anoxic cellular environment thereby switching the signal on in case of hypoxia.

An additional fluorescence microscopy experiment was designed, where the emission was observed in the visible region, but excitation was performed in the NIR by a simple diode laser in an inverted fluorescence microscope (Fig. S9, ESI†). This experiment demonstrated that luminescence recovery was possible even without the highly focused irradiation source of a confocal microscope. Further confirming UCNP-BDP-azo is a promising tool for the detection of hypoxia.

Conclusions

In this study, a hypoxia-responsive upconversion nanosensor was developed. The probe was obtained *via* an EDC/NHS coupling reaction between the UCNP and the hypoxia-sensitive azo dye. The optimised probe exhibited a negligible fluorescence signal in the visible region under normal conditions. However, chemical reduction experiments, as well as cellular anoxia experiments for the creation of a reductive environment, demonstrated that the reduction of the azo bond was possible, and that quenching could be stopped. Confocal fluorescence microscopy confirmed that UCNP-BDP-azo were localised inside the cells and recuperated emissions in the visible region stemming from upconversion when exposed to a hypoxic

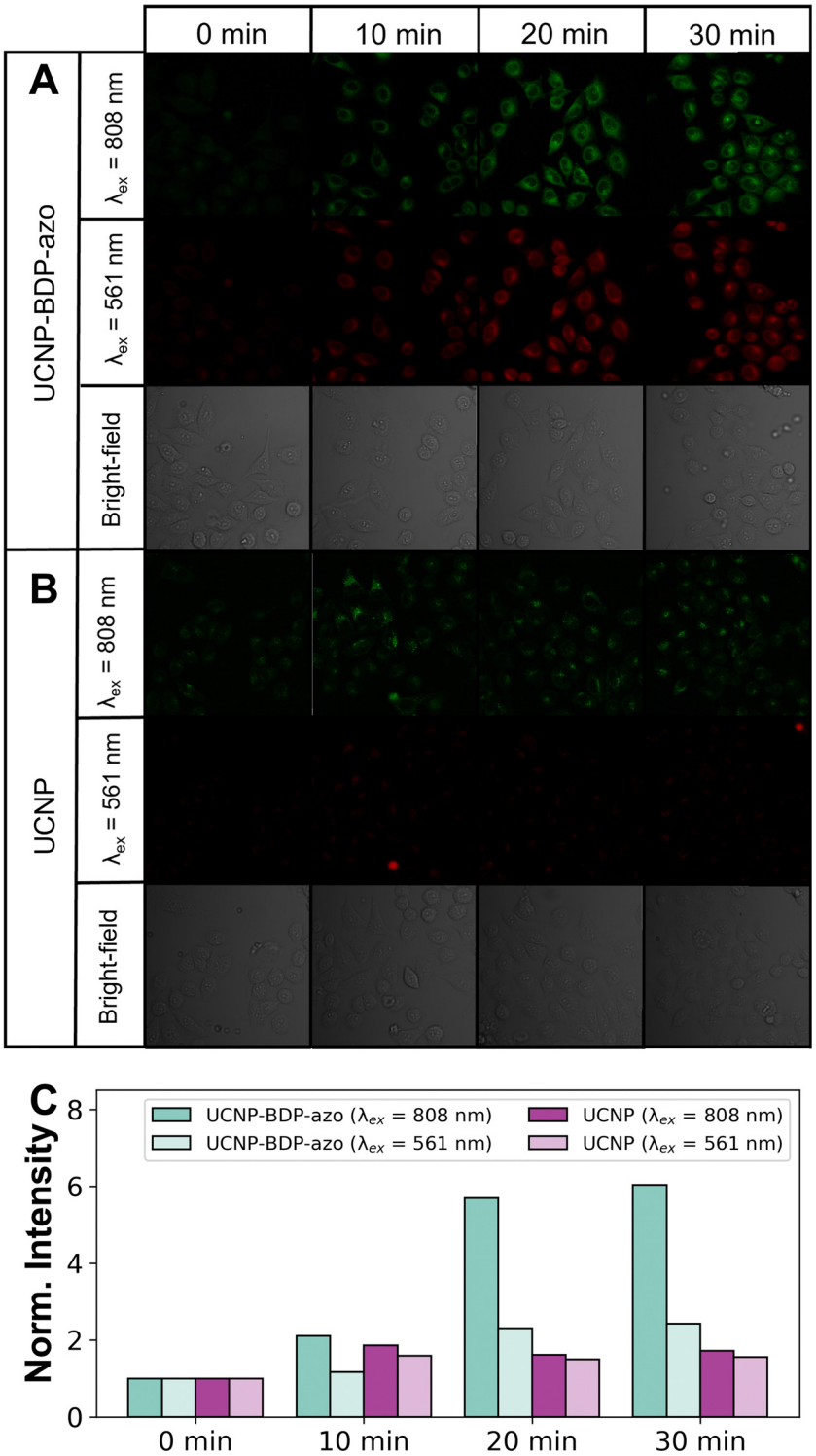

Fig. 5 Confocal microscope images showing the hypoxic response in sealed HeLa cell cultures of (A) UCNP-BDP-azo, where the first two rows present two different excitation channels and the third the bright-field view and (B) UCNP (3 middle rows). (C) Representation of the increase in intensity over time obtained from the images in (A) and (B) showing the increase in intensity for the cells incubated with UCNP-BDP-azo under anoxia over time.

environment. Additionally, the UCNP-BDP-azo probe maintained their NIR-emission independently of the azo-bond, conferring the particles with the capability to act as contrast agent in deep-tissue imaging. Therefore, the developed nanosensor was revealed to be a promising probe for detecting hypoxic environments that includes tracking capability owing to its maintained NIR emissions. Future work will focus on more hypoxia-sensitive organic dyes that could show improved

solubility and liberation of the BDP-NH_2 dye after reduction of the azo bond to improve recovery from quenching.

Author contributions

J. Yao: investigation, data curation; S. Simon: investigation, data curation; G. Lopez-Peña: data curation, visualization, writing; S. Gómez-Pastor: investigation; S. Guisan-Ceinos: investigation; R. Marin: supervision, visualization, writing, resources, funding; E. Martín Rodríguez: methodology, formal analysis, writing, funding; D. Jaque: conceptualization, methodology, funding, resources; F. Sanz-Rodríguez: investigation, data curation, visualization, resources, funding, writing; M. Ribagorda: supervision, methodology, resources, funding, writing D. H. Ortgies: supervision, methodology, resources, funding, writing.

Data availability

The authors declare that the data supporting this article will be made available at **https://zenodo.org/**.

Conflicts of interest

There are no conflicts to declare.

Acknowledgements

This work was financed by the Spanish Ministerio de Ciencia e Innovación MCIN/AEI/10.13039/501100011033 under projects PID2019-106211RB-I00 (nanonerv), PID2020-113059GB-C22, PID2020-118878RB-I00 (RETINanoTHERMIA) and PID2023-146801NB-C32, by the Instituto de Salud Carlos III (PI19/00565), by the Comunidad Autónoma de Madrid (CAM) S2022/BMD-7403 RENIM-CM grant and co-financed by the European structural and investment fund. Additional funding was provided by the European Union Horizon 2020 FETOpen project NanoTBTech (801305), the Comunidad Autónoma de Madrid and Universidad Autónoma de Madrid young investigator project SI3/PJI/2021-00211, the Fundación para la Investigación Biomédica del Hospital Universitario Ramón y Cajal projects IMP21_A4 (2021/0427) and IMP18_38 (2018/0265), and also by COST action CA17140. R. M. acknowledges the support of the European Union's Horizon 2020 research and innovation program under the Marie Skłodowska-Curie Grant Agreement no. 797945 (LANTERNS), and is grateful to the Spanish Ministerio de Ciencia, Innovación y Universidades for support to research through a Ramón y Cajal Fellowship (RYC2021-032913-I) and Project PID2022-14210NA-I00 (NAMASTEPS) funded by MCIN/AEI/10.13039/501100011033 and by FEDER, EU. J. Y. acknowledges the support from the China Scholarship Council (CSC File no. 201704910867). D. H. O. is grateful for Ramón y Cajal Fellowship RYC2022-036732-I funded by MCIN/AEI/10.13039/501100011033 and by "ESF investing in your future". E. M. R. and D. H. O. acknowledge Grant CPP2021-008902 funded by MCIN/AEI/10.13039/501100011033 and by the "European Union NextGenerationEU/PRTR". Silvia Gómez-Pastor is a predoctoral fellow of the Autonomous Community of Madrid (Grant PIPF-2022/SAL-GL-25806). We thank the "Unidad de Microscopía e Imagen Dinámica del Centro Nacional de Investigaciones Cardiovasculares Carlos III" facility for their assistance and are grateful to Paloma Rodríguez Sevilla for help with the group's microscopes.

Notes and references

1 M. C. Brahimi-Horn, J. Chiche and J. Pouysségur, *J. Mol. Med.*, 2007, **85**, 1301–1307.
2 M. V. Blagosklonny, *Cancer Cell*, 2004, **5**, 13–17.
3 O. Trédan, C. M. Galmarini, K. Patel and I. F. Tannock, *J. Natl. Cancer Inst.*, 2007, **99**, 1441–1454.
4 P. Vaupel, K. Schlenger, C. Knoop and M. Höckel, *Cancer Res.*, 1991, **51**, 3316–3322.
5 E. E. Verwer, R. Boellaard and A. A. van der Veldt, *World J. Clin. Oncol.*, 2014, **5**, 824–844.
6 X. Lin, Q. Ruan, L. Lin, X. Zhang, X. Duan, Y. Teng and J. Zhang, *J. Radioanal. Nucl. Chem.*, 2018, **317**, 1463–1468.
7 L. Ge, Y. Tang, C. Wang, J. Chen, H. Mao and X. Jiang, *Nat. Commun.*, 2024, **15**, 153.
8 X.-B. Zhao, J.-Y. Kang and Y.-P. Shi, *Anal. Chem.*, 2022, **94**, 6574–6581.
9 S. Acharya and R. Misra, *Nanomedicine*, 2022, **42**, 102549.
10 A. L. D. Wallabregue, H. Bolland, S. Faulkner, E. M. Hammond and S. J. Conway, *J. Am. Chem. Soc.*, 2023, **145**, 2572–2583.
11 L. Gai, Y. Liu, Z. Zhou, H. Lu and Z. Guo, *Coord. Chem. Rev.*, 2023, **481**, 215041.
12 J. Liu, W. Bu and J. Shi, *Chem. Rev.*, 2017, **117**, 6160–6224.
13 G. G. Dias, A. King, F. de Moliner, M. Vendrell and E. N. da S. Júnior, *Chem. Soc. Rev.*, 2018, **47**, 12–27.
14 H. Komatsu, Y. Shindo, K. Oka, J. P. Hill and K. Ariga, *Angew. Chem., Int. Ed.*, 2014, **53**, 3993–3995.
15 S. Karan, M. Y. Cho, H. Lee, H. Lee, H. S. Park, M. Sundararajan, J. L. Sessler and K. S. Hong, *J. Med. Chem.*, 2021, **64**, 2971–2981.
16 F. Xu, H. Li, Q. Yao, H. Ge, J. Fan, W. Sun, J. Wang and X. Peng, *Chem. Sci.*, 2019, **10**, 10586–10594.
17 Y. Li, Y. Sun, J. Li, Q. Su, W. Yuan, Y. Dai, C. Han, Q. Wang, W. Feng and F. Li, *J. Am. Chem. Soc.*, 2015, **137**, 6407–6416.
18 S. Karan, M. Y. Cho, H. Lee, H. M. Kim, H. S. Park, E. H. Han, J. L. Sessler and K. S. Hong, *J. Med. Chem.*, 2023, **66**, 14175–14187.
19 X. Meng, J. Zhang, Z. Sun, L. Zhou, G. Deng, S. Li, W. Li, P. Gong and L. Cai, *Theranostics*, 2018, **8**, 6025–6034.
20 Y. Liu, W. Liu, H. Li, W. Yan, X. Yang, D. Liu, S. Wang and J. Zhang, *Anal. Chim. Acta*, 2018, **1024**, 177–186.
21 K. Morihiro, T. Ishinabe, M. Takatsu, H. Osumi, T. Osawa and A. Okamoto, *J. Am. Chem. Soc.*, 2021, **143**, 3340–3347.
22 R. Zou, Q. Gong, Z. Shi, J. Zheng, J. Xing, C. Liu, Z. Jiang and A. Wu, *Nanoscale*, 2020, **12**, 14870–14881.
23 X. Tian, Z. Li, Y. Sun, P. Wang and H. Ma, *Anal. Chem.*, 2018, **90**, 13759–13766.

24 A. Chevalier, P. Y. Renard and A. Romieu, *Chem. – Asian J.*, 2017, **12**, 2008–2028.
25 W. Piao, S. Tsuda, Y. Tanaka, S. Maeda, F. Liu, S. Takahashi, Y. Kushida, T. Komatsu, T. Ueno, T. Terai, T. Nakazawa, M. Uchiyama, K. Morokuma, T. Nagano and K. Hanaoka, *Angew. Chem., Int. Ed.*, 2013, **52**, 13028–13032.
26 W. Liu, X. Yao, W. Zhu, J. Wang, F. Zhou, X. Qian, A. Tiemuer, S. Yang, H.-Y. Wang and Y. Liu, *ACS Appl. Bio Mater.*, 2021, **4**, 2752–2758.
27 N. Ding, Z. Li, X. Tian, J. Zhang, K. Guo and P. Wang, *Chem. Commun.*, 2019, **55**, 13172–13175.
28 S. Yao, Y. Chen, H. Xu, F. Qi, Y. Zhang, T. Yang, Y. Wu, H. Fang, W. He and Z. Guo, *Dyes Pigm.*, 2022, **206**, 110583.
29 J. Xiong, P. Wang, S. Son, C. Zhong, F. Zhang, Z. Mao, Z. Liu and J. S. Kim, *Matter*, 2022, **5**, 1502–1519.
30 C. Wang, S. Wang, Y. Wang, H. Wu, K. Bao, R. Sheng and X. Li, *Sci. Rep.*, 2020, **10**, 12127.
31 D. Xiao, L. Liu, F. Xie, J. Dong, Y. Wang, X. Xu, W. Zhong, H. Deng, X. Zhou and S. Li, *Angew. Chem., Int. Ed.*, 2024, **63**, e202310318.
32 H. Liu, X. Zeng, H. Yin, J. Chen, W. Xie, G. Zhou, G. Mao, Y. Zhou and S. Yang, *Sens. Actuators, B*, 2023, **381**, 133431.
33 A. Chevalier, C. Massif, P.-Y. Renard and A. Romieu, *Chem. – Eur. J.*, 2013, **19**, 1686–1699.
34 K. Kiyose, K. Hanaoka, D. Oushiki, T. Nakamura, M. Kajimura, M. Suematsu, H. Nishimatsu, T. Yamane, T. Terai, Y. Hirata and T. Nagano, *J. Am. Chem. Soc.*, 2010, **132**, 15846–15848.
35 T. Myochin, K. Hanaoka, T. Komatsu, T. Terai and T. Nagano, *J. Am. Chem. Soc.*, 2012, **134**, 13730–13737.
36 G. López-Peña, S. Simón-Fuente, D. H. Ortgies, M. Á. Moliné, E. Martín Rodríguez, F. Sanz-Rodríguez and M. Ribagorda, *Cancers*, 2023, **15**, 102.
37 J. Wu, J. Wu, W. Wei, Y. Zhang and Q. Chen, *Small*, 2024, **20**, 2311729.
38 X. Zhang, W. Shu, M. Cheng, L. Wang and X. Ran, *Nanotechnology*, 2023, **34**, 415502.
39 S. Xu, X. Zhang, H. Xu, B. Dong, X. Qu, B. Chen, S. Zhang, T. Zhang, Y. Cheng, S. Xu and H. Song, *Sci. Rep.*, 2016, **6**, 22350.
40 J. Liu, Y. Liu, W. Bu, J. Bu, Y. Sun, J. Du and J. Shi, *J. Am. Chem. Soc.*, 2014, **136**, 9701–9709.
41 S. Guisán-Ceinos, A. R. Rivero, F. Romeo-Gella, S. Simón-Fuente, S. Gómez-Pastor, N. Calvo, A. H. Orrego, J. M. Guisán, I. Corral, F. Sanz-Rodriguez and M. Ribagorda, *J. Am. Chem. Soc.*, 2022, **144**, 8185–8193.
42 N. Shin, K. Hanaoka, W. Piao, T. Miyakawa, T. Fujisawa, S. Takeuchi, S. Takahashi, T. Komatsu, T. Ueno, T. Terai, T. Tahara, M. Tanokura, T. Nagano and Y. Urano, *ACS Chem. Biol.*, 2017, **12**, 558–563.
43 F. Wang, R. Deng and X. Liu, *Nat. Protoc.*, 2014, **9**, 1634–1644.
44 F. Wang, R. Deng, J. Wang, Q. Wang, Y. Han, H. Zhu, X. Chen and X. Liu, *Nat. Mater.*, 2011, **10**, 968–973.
45 X. Zhang, Z. Zhao, X. Zhang, D. B. Cordes, B. Weeks, B. Qiu, K. Madanan, D. Sardar and J. Chaudhuri, *Nano Res.*, 2015, **8**, 636–648.
46 F. Wang, J. Wang and X. Liu, *Angew. Chem., Int. Ed.*, 2010, **49**, 7456–7460.
47 A. Skripka, A. Benayas, C. D. S. Brites, I. R. Martín, L. D. Carlos and F. Vetrone, *Nano Lett.*, 2020, **20**, 7648–7654.
48 M. Danaei, M. Dehghankhold, S. Ataei, F. Hasanzadeh Davarani, R. Javanmard, A. Dokhani, S. Khorasani and M. R. Mozafari, *Pharmaceutics*, 2018, **10**, 57.
49 V. Muhr, S. Wilhelm, T. Hirsch and O. S. Wolfbeis, *Acc. Chem. Res.*, 2014, **47**, 3481–3493.
50 V. Muhr, C. Würth, M. Kraft, M. Buchner, A. J. Baeumner, U. Resch-Genger and T. Hirsch, *Anal. Chem.*, 2017, **89**, 4868–4874.
51 G. B. Kauffman, *J. Chem. Educ.*, 1988, **65**, 28–31.
52 J. Bart, R. Tiggelaar, M. Yang, S. Schlautmann, H. Zuilhof and H. Gardeniers, *Lab Chip*, 2009, **9**, 3481.
53 L. Wu, C. Huang, B. P. Emery, A. C. Sedgwick, S. D. Bull, X.-P. He, H. Tian, J. Yoon, J. L. Sessler and T. D. James, *Chem. Soc. Rev.*, 2020, **49**, 5110–5139.
54 M. Tan, B. Del Rosal, Y. Zhang, E. Martín Rodríguez, J. Hu, Z. Zhou, R. Fan, D. H. Ortgies, N. Fernández, I. Chaves-Coira, Á. Núñez, D. Jaque and G. Chen, *Nanoscale*, 2018, **10**, 17771–17780.
55 Y. Wang, K. Liu, X. Liu, K. Dohnalová, T. Gregorkiewicz, X. Kong, M. C. G. Aalders, W. J. Buma and H. Zhang, *J. Phys. Chem. Lett.*, 2011, **2**, 2083–2088.
56 S. Bhuckory, E. Hemmer, Y. Wu, A. Yahia-Ammar, F. Vetrone and N. Hildebrandt, *Eur. J. Inorg. Chem.*, 2017, 5186–5195.
57 E. Takahashi and M. Sato, *Am. J. Physiol.*, 2010, **299**, C1318–C1323.